

CFD modelling of biomass catalytic fast pyrolysis in bubbling fluidized reactor: effects of catalyst parameters on process performance

Yajun Qiu^a, Qixiang Xu^{b*}, Shusheng Pang^{c,d}, Xiaoyuechuan Ma^e

^aPatent Examination Cooperation (Henan) Center of the Patent Office, China

^bCollege of Ecological and Environmental Engineering, Zhengzhou University,
Zhengzhou, China

^cDepartment of Chemical & Process Engineering, Canterbury University, NZ

^dHenan Centre for Outstanding Overseas Scientists, Zhengzhou University, Zhengzhou,
China

^eCollege of Chemical Engineering, Zhengzhou University, Zhengzhou, China

*: Corresponding author: xuqixiang@zzu.edu.cn

Abstract

In this study, a CFD mathematical model has been developed for catalytic fast pyrolysis (CFP) of biomass based on multi-phase flow, transfer process and biomass pyrolysis reactions in a bubbling fluidized bed reactor. The multi-phase fluid flow, and the inter-phase momentum and energy transfer processes are modelled with Eulerian multi-phase formulas, representing the flows of gases and solids (catalyst and biomass) within the reactor. The biomass catalytic fast pyrolysis reactions are described by using a two-stage, semi-global model. Specified secondary tar catalytic cracking process, which considers both intrinsic reaction rates and mass transfer process, is embedded to the developed model by user-defined function (UDF). The model simulation results of pyrolysis product yield and distribution are compared with the experimental data with close agreement. The model is then employed to

This article has been accepted for publication and undergone full peer review but has not been through the copyediting, typesetting, pagination and proofreading process which may lead to differences between this version and the [Version of Record](#). Please cite this article as doi: [10.1002/aic.17637](https://doi.org/10.1002/aic.17637) © 2022 American Institute of Chemical Engineers
Received: Sep 01, 2021; Revised: Dec 23, 2021; Accepted: Jan 30, 2022

investigate the effects of structural properties of catalyst, such as specific internal area, average size of active sites, pore diameter, and tortuosity, on products yields and composition. The tar cracking process by the selected catalyst is proposed and the influences of adsorption capability of tar molecule on catalyst surface and external film mass transfer are also analyzed. The developed model can be solved with short computational time and thus it can be employed for further research and engineering designs of the catalytic pyrolysis of carbonaceous materials.

Key words: CFD, biomass, catalytic fast pyrolysis, catalyst structural properties, bubbling fluidized bed, multiphase flow, mass & energy transfer, multi-step reactions.

1. Introduction

Fast pyrolysis of biomass is thermal decomposing of biomass into solid char, non-condensable and condensable volatile substances in the absence of oxygen. In general, the non-condensable gases mainly consist of CO, CO₂, CH₄ and H₂ while condensable volatiles become liquid when being cooled down, and thus are often referred to as bio-oil or liquid product^{1,2}. Fast pyrolysis of biomass normally operates in the temperature range from 450 to 600 °C to maximize liquid yield^{3,4}. However, bio-oil produced from traditional fast pyrolysis has several adverse properties such as high oxygen content and acidity, low calorific value, low stability and ease of polymerization, all of which restrict applications of the raw bio-oil⁵. Therefore, the common approach is to upgrade the raw bio-oil, such as by hydro-deoxygenation, to improve the bio-oil quality. The hydro-deoxygenation upgrading process operates at high pressures and elevated temperatures, and thus the process is complicated.

Accepted Article

Alternative pathway to improve the bio-oil quality is to apply appropriate catalysts in the pyrolysis process in which the undesirable compounds are cracked and hydrocarbon-concentrated compounds are obtained through phase separation⁶. This catalytic fast pyrolysis process (hereinafter referred to as CFP) of biomass operates at atmospheric pressure and at normal range of temperatures, therefore the process is less expensive in comparison with two steps approach of fast pyrolysis followed by upgrading. The CFP has recently attracted increasing interests in biomass thermochemical conversion, however, reports on detailed reactions and reaction kinetics in the catalytic fast pyrolysis of biomass have not been found in literature.

The computational fluid dynamics (CFD) modelling can precisely predict the coupling physical and chemical processes in a multiphase flow system. Insight and foresight simulation by the CFD modelling enables to gain fundamental understanding of the simulated process, such that expensive and time-consuming experiments can be minimized or even avoided. CFD has been widely used in the thermochemical conversion processes of biomass including combustion^{7,8}, gasification⁹⁻¹¹, pyrolysis¹² and bio-oil upgrading^{13,14}. CFD modeling of biomass fast pyrolysis in bubbling or circulating fluidized bed has also been reported^{1,12,15-23} in which the impacts of operating conditions, heat and mass transfers and biomass properties on the pyrolysis reactions were studied. Dong²⁴ developed a CFD model to simulate both the non-catalytic and the catalytic pyrolysis of woody biomass in a lab-scaled bubbling fluidized bed and found that the use of catalytic bed materials could change the pyrolysis product distribution. The model used a simple secondary

Accepted Article

reaction mechanism of bio-oil vapor in the catalyst bed, and the reaction rate was only related to weight hourly space velocity (WHSV) of catalyst to tar. Sun et al.²⁵ simulated the CFP of sawdust with ZMS-5 zeolite catalyst in a circulating fluidized bed reactor which was used to predict the product distribution at different WHSVs of catalyst to biomass feedstock. The results showed that the gas yield increased and the liquid yield decreased with the increase in catalyst loading, which are in consistency with the general trends of experimental results. In the above two models, the CFP reaction rates were assumed to be exponential functions of macro-scale factor of WHSV of catalyst to tar vapor. However, micro-scale factors, which may also play an important role in the biomass CFP, were not considered in the above models, therefore, the effects of catalyst structural properties and internal energy and mass transfer process cannot be assessed.

In this work, a novel CFD model has been developed to simulate the biomass CFP in a bubbling fluidized bed reactor. Micro-scale factors including catalyst specific surface area, pore size and tortuosity, and intra-particle diffusion of tar are incorporated into the secondary tar cracking reaction process. To our best knowledge, this is the first attempt to evaluate the impacts of micro-level properties of the catalyst and the combination of catalyst micro-structural properties with internal mass transfer on the biomass CFP process. The developed model has been solved by CFD code ANSYS Fluent 16.2 and the proposed comprehensive reaction mechanism was embedded into the model by user-defined function (UDF). Impacts of catalyst structural properties and mass transfer, which are difficult to alter in real experiments,

on the biomass CFP performance have been investigated in the present study.

2. Model Formulation and Solution Method

2.1 Scope of the study

The proposed CFD model was developed to simulate a lab-scale bubbling fluidized bed pyrolysis reactor as shown in Fig. 1 with biomass feeding rate of 2 kg/h and catalyst loading height of 80 mm. This reactor has the same configuration and dimensions as the laboratory-scale pyrolysis reactor, on which experiments for model validation were conducted in the present study. The details of this reactor system have been reported previously⁴⁰. However, once the model is validated, it can be employed to simulate larger scale reactors by modifying the reactor geometry. In the simulated catalytic pyrolysis, nitrogen, as the heating and fluidization medium, was injected from the bottom of the reactor and penetrates through the catalyst bed with a superficial velocity of $U_0 = 0.3$ m/s, and the reactor temperature was maintained at 773 K by isothermal settings of the heating medium and the electric heating on the wall. The superficial velocity was approximately 3 times of the minimum fluidizing velocity, U_{mf} , corresponding to the selected catalyst diameter. Pine sawdust was selected as the biomass feedstock, which was introduced from the left side at height of 40mm above the bottom of the reactor. The control volume for the simulation is the expanded bed with bubbling fluidization as shown in Fig.1.

(Insert Fig. 1 here)

Hydrodynamic behaviors including phase coupling, momentum exchange and disengagement of gas-catalyst-biomass multi-phase flow, were modelled by using three Eulerian phases with gas as the primary and continuous phase, and solids

(biomass and catalyst) as the secondary phases. Such approach has been frequently used for thermochemical conversion of biomass in fluidized bed reactors^{12,17}. For the inter-phase momentum exchange, only drag force is considered since it is the dominant term in this case. The average diameters of catalyst and biomass particles were set to be 0.5 mm, and the granules of such size belong to Geldart B Group²⁶.

In order to simplify the model, the following assumptions have been made: (1) the biomass feedstock contains no free moisture hence the drying process is not considered in the modelling; (2) ideal gas law has been applied to the gas mixture as the reactor operates at atmospheric pressure; (3) The catalyst and the biomass particles are spherical and uniform in diameter. (4) The pre-determined CFP reactions kinetic parameters and stoichiometry constants are not affected by catalyst structural properties in sensitivity studies.

2.2 Mass conservation equations

The continuity equation for each Eulerian phase that simulates the hydrodynamics of gas-catalyst-biomass system is²⁷:

$$\frac{\partial}{\partial t}(\alpha\rho) + \nabla \cdot (\alpha\rho\vec{v}) = \dot{m} + S \quad (1)$$

where α is the phase volume fraction (-), ρ is the density (kg/m³), \dot{m} represents total mass exchange rate between the phases (kg/m³/s), S is the user defined mass source term (kg/m³/s).

Equation (2) is for mass conservation of each component in the gas phase²⁷:

$$\frac{\partial}{\partial t}(\alpha_g\rho_g Y_i) + \nabla \cdot (\alpha_g\rho_g\vec{v}_g Y_i) = \dot{m}_g + S_g \quad (2)$$

where Y_i is the mass fraction of i^{th} specie in gas phase (-).

2.3 Momentum conservation and inter-phase exchange equations

In the bubbling fluidized bed to be simulated, gas flow rate is not sufficiently enough to reach turbulent flow regime, thus the laminar viscous model is selected.

The momentum conservative equation for the primary gas phase is developed as follows²⁷:

$$\frac{\partial}{\partial t}(\alpha_g \rho_g \vec{v}_g) + \nabla \cdot (\alpha_g \rho_g \vec{v}_g \vec{v}_g) = -\alpha_g \nabla p + \nabla \cdot \bar{\tau}_g + \alpha_g \rho_g \mathbf{g} + K_{gs}(\vec{v}_g - \vec{v}_s) + K_{gw}(\vec{v}_g - \vec{v}_w) + \dot{m}_{gw} \vec{v}_g \quad (3)$$

where p is pressure (Pa), $\bar{\tau}_g$ is the viscous stress tensor, \mathbf{g} is the gravitational force (9.81 m/s²), K_{gs} , K_{gw} are the phase momentum exchange coefficient for gas-solid phases (kg/m³/s), $\dot{m}_{gw} \vec{v}_g$ is the momentum transfer term associated to mass transfer between gas and biomass (kg/m²/s²), $K_{gs}(\vec{v}_g - \vec{v}_s)$ and $K_{gw}(\vec{v}_g - \vec{v}_w)$ are the interphase forces for the coupling of gas and solid momentum equations by drag forces (kg/m²/s²). The momentum conservative equations of the two secondary phases are similar to the gas phase.

The Gidaspow model²⁸ that is valid for dense phase momentum exchange is used to calculate the drag force between gas and catalyst:

$$K_{gs} = \frac{3\alpha_s \alpha_g \rho_g}{4v_{r,s}^2 d_s} C_D \left(\frac{Re_s}{v_{r,s}} \right) |\vec{v}_s - \vec{v}_g| ; C_D = \left(0.63 + \frac{4.8}{\sqrt{Re_s/v_{r,s}}} \right)^2 \quad (4)\&(5)$$

Re_s , Reynolds number of solids relative to gas phase and $v_{t,s}$, terminal velocity correlation for the solid phase are calculated as:

$$Re_s = \frac{\rho_g d_s |\vec{v}_s - \vec{v}_g|}{\mu_1} \quad (6)$$

$$v_{t,s} = 0.5 \left(A - 0.06 Re_s + \sqrt{(0.06 Re_s)^2 + 0.12 Re_s (2B - A) + A^2} \right) \quad (7)$$

where A and B are the parameters relate to gas phase fraction:

$$A = \alpha_g^{4.14}, \quad B = \begin{cases} 0.8 \alpha_g^{1.28}, & \alpha_g \leq 0.85 \\ \alpha_g^{2.65}, & \alpha_g > 0.85 \end{cases} \quad (8)\&(9)$$

Wen-Yu model²⁹ is used for drag force between the biomass and gas as shown in Equation (10) and the drag coefficient is determined by Equation (11) as follows:

$$K_{gw} = \frac{3}{4} C_D \frac{\alpha_w \alpha_g \rho_g |\vec{v}_w - \vec{v}_g|}{d_s} \alpha_g^{-2.65}; \quad C_D = \frac{24}{\alpha_g Re_s} \left[1 + 0.15 (\alpha_g Re_s)^{0.687} \right] \quad (10)\&(11)$$

The drag force between the catalyst and biomass is described with solid-solid drag model. The expression of momentum exchange coefficient K_{ws} is given by Equation (12), and e_{sw} is coefficient of restitution, which is set to 0.9. $C_{fr,sw}$ represents the friction coefficient between catalyst and biomass, and d_w is the biomass particle diameter. $g_{0,sw}$ is the radial distribution function, calculated according to Syamlal et al.³⁰:

$$K_{ws} = \frac{3(1 + e_{sw}) \left(\frac{\pi}{2} + C_{fr,sw} \frac{\pi^2}{8} \right) \alpha_s \rho_s \alpha_w \rho_w (d_w + d_s)^2 g_{0,sw}}{2\pi(\rho_b d_w^3 + \rho_s d_s^3)} |\vec{v}_s - \vec{v}_w| \quad (12)$$

2.3 Energy conservation and inter-phase exchange equations

In the bubbling fluidized bed to be simulated, both conductive and convective heat transfers have been considered, while radiation is insignificant thus is not taken

in account. The energy conservation equation for the gas phase is expressed as follows:

$$\frac{\partial}{\partial t}(\alpha_g \rho_g h_g) + \nabla \cdot (\alpha_g \rho_g \vec{v}_g h_g) = -\alpha_g \frac{\partial p}{\partial t} + \bar{\tau}_g : \nabla \vec{v}_g - \nabla \cdot \vec{q}_g + S + h_{gs} a_{gs} (T_g - T_s) + h_{gw} a_{gw} (T_g - T_w) \quad (13)$$

where h_{gs} and h_{gw} stand for heat transfer coefficients of the gas-catalyst, gas-biomass pairs. a_{gw} and a_{gs} represent the interfacial area concentrations between gas and biomass and between gas and catalyst, respectively.

The heat transfer between gas and catalyst uses the model developed by Gunn et al.³²: $h_{gs} = \frac{6\lambda_g \alpha_g \alpha_s Nu_s}{d_s^2}$

$$(14)$$

where λ_g is the thermal conductivity coefficient of the gas, and Nu_s is the solids Nusselt number, which can be expressed by:

$$Nu_s = (7 - 10\alpha_g + 5\alpha_g^2) \left(1 + 0.7Re_s^2 Pr_s^{\frac{1}{3}}\right) + (1.33 - 2.4\alpha_g + 1.2\alpha_g^2) Re_s^{0.7} Pr_s^{\frac{1}{3}} \quad (15)$$

Prandtl number (Pr) is determined as: $Pr = \frac{C_{p,g} \mu_g}{\lambda_g}$

$$(16)$$

Heat transfer rate between the gas phase and the biomass phase is dominant on the rates of pyrolysis reactions although the heat transfer between catalyst and biomass can also make contribution to a certain extent. Energy required for the endothermic biomass pyrolysis reactions comes from the convective heat transfer from the gas phase, which coefficient is calculated using the Ranz - Marsha model³³ as given in Equations (17) and (18). The heat transfer between catalyst and biomass is calculated by Equation (19).

$$h_{gw} = \frac{\lambda_g Nu_w}{d_w}; Nu_w = 2.0 + 0.15 Re_w^{0.8} Pr^{0.5}; h_{sw} = \sqrt{\frac{C_{p_s} \lambda_s \rho_s \alpha_s^2}{\pi t}} \quad (17)&(18)&(19)$$

2.3 Reaction pathways and kinetics of biomass catalytic fast pyrolysis

(Insert Fig.2 here)

The reaction pathway scheme and kinetics of biomass catalytic fast pyrolysis are proposed as shown in Fig. 2 using a two-stage, semi-global mechanism^{1,34,35} in which ‘oil’ represents the organic components in the organic phase and ‘aqua’ the aqueous phase in the liquid product, respectively. All of the primary pyrolysis reactions with kinetic coefficients of k_1 to k_3 are assumed to be in first order which can be expressed by the Arrhenius kinetics equation (Equation 20). The values of the kinetic parameters are obtained from Blasi et al.³⁶ as given in Table 1.

$$k_i = A_i \exp\left(-\frac{E_{a,i}}{RT}\right) \quad (20)$$

(Insert Table 1 here)

The rate of secondary catalytic cracking reaction of tar, which incorporates catalyst properties and mass transfer effects, will be introduced in the following section.

2.4 Catalytic tar cracking mechanism

The catalytic secondary tar cracking reaction is the key reaction in improving bio-oil quality in the pyrolysis process. Therefore, this reaction is an important part in the CFP model which takes into account the effects of catalyst structural properties and mass transfer between the tar components and the catalyst. The catalyst structural properties include porosity, specific surface area, pore diameter, curvature and

adsorption coefficient of tar on the catalyst surface. Both external mass transfer of the tar vapor from bulk gas phase to outer surface of catalyst and internal diffusion through catalyst pores have been considered.

The overall volumetric rate of tar catalytic cracking in each cell, R_{real} , is given as:

$$R_{\text{real}} = R_{\text{max}} \eta f_{mt} \varepsilon_{\text{cata}} \quad (21)$$

Where R_{max} is the maximum possible volumetric reaction rate throughout the catalyst particle corresponding to concentrations of bulk gas phase species, and η is the effective factor which is defined as the ratio of the volume-averaged reaction rate to R_{max} . f_{mt} in the above equation is the external mass transfer factor defined as ratio of tar concentration at apparent surface of the catalyst particles to the bulk gas phase, and $\varepsilon_{\text{cata}}$ is the mean catalyst volume fraction of each cell in the fluidized bed.

The maximum possible volumetric reaction rate, R_{max} , can be calculated by:

$$R_{\text{max}} = A e^{\frac{E_a}{RT}} C_{\text{TS}} \theta_{\text{tar}} = A e^{\frac{E_a}{RT}} \frac{S}{D_{AC}^2 NA} K_a p_{\text{tar}} \quad (22)$$

The above equation is used to calculate the theoretical maximum volumetric rate of catalytic tar cracking reaction throughout a catalyst particle volume which is a function of catalyst properties and surrounding tar partial pressure around the catalyst particle. In the above equation, S is the specific surface area of the catalyst particles, D_{AC} is the average size of the active site of the catalyst (the active site is approximately the square shaped, NA represents Avogadro constant, K_a is the adsorption coefficient of tar molecules on the catalyst surface, and p_{tar} is the partial pressure of tar in the main gas phase.

The effect of the internal diffusion of gaseous species within a catalyst particle

was estimated by effective reaction volume method. The effective factor, η , is defined as the ratio of the volume-averaged reaction rate to the maximum reaction rate that could be determined while the internal diffusion rate is assumed infinity. η is an unique function of Thiele modulus, ϕ , which is the dimensionless ratio of intrinsic gas-solid reaction to internal diffusion rate. For spherical catalyst particles, η is determined by the correlation:

$$\eta = \frac{1}{V_s R(C_{i,\max})} \int_{V_{\text{cata}}} R(C_i) dV = \frac{1}{3\phi^2} \left(\frac{3\phi}{\tanh(3\phi)} - 1 \right) \quad (23)$$

$$\text{in which } \phi = \frac{d_p}{6} \sqrt{\frac{k_{\text{ap}}}{D_{\text{tar}}^{\text{eff}}}} \quad (24)$$

where d_p is the average diameter of catalyst particles. k_{ap} is the apparent reaction kinetic constant in first order approximation which can be expressed by:

$$k_{\text{ap}} = R_{\text{max}}/C_{\text{tar}} \quad (25)$$

In Equation (24), $D_{\text{tar}}^{\text{eff}}$ represents the effective diffusivity of tar molecules in the internal pore of catalyst particles, which is estimated by using the Bosanquet formula:

$$D_{\text{tar}}^{\text{eff}} = \frac{\varepsilon}{\tau} \left(\frac{1}{D_{\text{tar,m}}} + \frac{1}{D_{\text{tar,Kn}}} \right)^{-1} \quad (26)$$

In the above equation, $D_{\text{tar,m}}$ is the free-space diffusivity of tar in gas phase, and $D_{\text{tar,Kn}}$ is the Knudsen diffusivity in pores. These parameters are evaluated from binary diffusivities and catalyst pore diameter:

$$D_{\text{tar,m}} = \frac{1}{1-x_{\text{tar}}} \sum_{\substack{j=1 \\ j \neq \text{tar}}}^n D_{\text{tar,j}}^b X_j \quad ; \quad D_{\text{tar,Kn}} = \frac{d_{\text{pore}}}{3} \sqrt{\frac{8RT}{\pi MW_{\text{tar}}}} \quad (27)\&(28)$$

The average diameter of the catalyst pore is estimated by the assumption of cylindrical geometry, and effect of pore curvature is taken into account by tortuosity factor τ as shown in Equation (26).

$$d_{\text{pore}} = \frac{4\varepsilon}{S_0} \quad (29)$$

The external mass transfer correction factor, f_{mt} , represents the effect of mass transfer resistance from bulk gas phase to the outer surface of the catalyst particles which is calculated by letting the overall consumption rate of tar throughout a catalyst particle, $\frac{\pi d_p^3}{6} k_{ap} C_{tar} f_{mt} \eta$, equal the external mass transfer rate from bulk gas to catalyst outer surface, $k \pi d_p^2 (C_{tar} - C_{tar} f_{mt})$. In this way, the reaction rate throughout the catalyst could be explicitly calculated from the gas phase tar concentration, and this will lead to the following equations.

$$f_{mt} = \left(1 + \frac{d_p k_{ap} \eta}{6k}\right)^{-1} \quad (30)$$

The film mass transfer coefficient on the catalyst outer surface, k , used in Equation (30) is calculated by the following equation³⁷.

$$k = \frac{D_{tar,m}}{d_p} (2 + 0.6 Re_s^{0.5} Sc^{1/3}) \quad (31)$$

Values of catalyst structural properties and kinetic constants of catalytic reaction (k_4) are listed in Table 2. The values of HZSM-5 properties used as the catalyst structural parameters are obtained from previous study³⁸. The activation energy for incomplete tar cracking, k_4 , takes the value from complete cracking³⁹, as the energy barrier for initiation of tar cracking is dominant in comparison to degradation of less stable intermediates.

(Insert Table 2 here)

2.5 Numerical strategies and solution procedures

The above developed CFP model was solved using a numerical technique in two dimensions for the bubbling fluidized bed reactor as shown in Fig.1. The reactor was

Accepted Article

discretized into a mesh of 48681 elements, with the mesh grid size ranging from $9.93 \times 10^{-7} \text{ m}^2$ to $1.0 \times 10^{-6} \text{ m}^2$ depending on the geometrical location. The coupled mass, momentum and energy conservative governing equations for each control volume were solved with ANSYS Fluent v16.2. Proposed secondary catalytic tar cracking process was embedded into the model by UDF compiled from source file written in C language. Heterogeneous Stiff Chemistry Solver was enabled for the purpose of enhanced numerical robustness of the simulation. Phase coupled SIMPLE was selected for solving pressure-velocity coupling, with first order upwind spatial discretization scheme. The under-relaxation factors in solving the governing equations used default values, with exception of 0.35 for momentum and 0.18 for volume fraction for better stability.

Prior to biomass feeding, a stable flow field of fluidizing gas at superficial velocity of 0.3 m/s in the catalyst bed at operation temperature of 500°C was obtained. After 2 s from the start, the pyrolysis started by setting biomass inlet feeding rate of 2 kg/h. Time step was initially set to be 10^{-4} second, and then fine-tuned during simulation to achieve convergence with least number of iterations over flow time advancing. Simulation continued until the concentration field of components became stable which was about 60 seconds from the start of biomass feeding. The average accumulated wall-clock time for simulation of 10 s pyrolysis process on a working station platform was approximately 33 hours.

2.6 Physical properties, and initial and boundary conditions

Initial conditions include the catalyst bed mass and height, nitrogen superficial velocity, biomass feeding rate and operating temperature. The reactor wall boundary was set as non-slippery with fixed-temperature. Detailed material properties, initial and boundary conditions in the model simulation are summarized in Table 3.

(Insert Table 3 here)

3. Results and Discussion

3.1. Model validation

The simulation results for product yields and distribution from the developed model of biomass catalytic fast pyrolysis (CFP) for the lab-scale bubbling fluidized bed pyrolyzer as shown in Fig.1 are presented in Fig.3, in which data of CFP of pine saw-dust for experimental validation of this work are also included for comparison. The experiments were conducted using bed materials of blended silicon sand and HZSM-5 zeolite catalyst at different blending ratios. Biomass particle size, catalyst and sand size, as well as the operation conditions were the same as those in the CFD model simulation listed in Table 2 and Table 3. In the simulation of CFP process with different blending ratios of catalyst to silica sand, these two solids were regarded as one Eulerian phase with physical properties based on the blending ratio and properties of catalyst and sand. In the meantime, the overall reaction rate of catalytic tar cracking was determined based on actual volume fraction of catalyst in bed.

Table 4 gives comparison among the simulation results from the proposed model

in this study (microscopic model), the results of CFP experiments conducted on same apparatus reported by this research team⁴⁰ and the simulation results using the macroscopic model as proposed by Dong²⁴. It was reported that the model proposed by Dong et al. could give predictions in close agreement with the experimental results⁴¹, however, the model tends to over-estimate the bio-oil yield but under-estimate the gas and char yields in comparison with the experimental results of this study. The close agreement of the simulation results from the model proposed in this study can be attributed to the inclusion of the secondary catalytic cracking of tars which is related to the microstructural properties of the catalyst.

(Insert Table 4 here)

From Table 4, it can be found that the product distributions predicted using the microscopic (developed in the present study) are in close agreement with the experimental data with discrepancies of -2.32% to 0.84% which are much less than the macroscopic model proposed by Dong et al. with discrepancies of -15.4% to 9.3%. The slight difference between the simulation results from the proposed microscopic CFP model and the experimental results may be due to the secondary thermal cracking reaction of tar which was not included in the CFD model although the thermal tar cracking is believed to be much less influential than the catalytic secondary tar cracking. However in the future work, the secondary thermal cracking reaction will also be integrated into the CFP model and the influence can then be quantitatively assessed.

Effects of catalyst blending ratio have also been examined by employing the

Accepted Article

developed CFP model and the simulation results are shown in Fig. 3 in which the experimental results are also included for comparison. From the figure, it can be found that the predicted product distributions are also in close agreement with the experimental data (overall $R^2 = 0.981$). Simulation results of the both models show that the liquid yield decreases while the gas and char yields increase with increasing the catalyst blending ratio. This trend is consistent with experimental results, therefore, it gives confidence that the developed CFP model can be employed to investigate the effects of microstructure properties of the catalyst on the product yields and product distribution from CFP of the biomass.

(Insert Fig. 3 here)

3.2. Detailed simulation results of biomass CFP in bubbling fluidized bed

With confidence in the developed model developed in the present study as discussed in the above section, the model has been employed to predict detailed information of the hydrodynamics, the temperature profile and the product distribution within the fluidized bed reactor.

3.2.1 Hydrodynamics of fluidized bed

(Insert Fig. 4 here)

Fig. 4 shows simulated volume fractions of three phases using the developed model for biomass CFP in the bubbling fluidized bed at steady operation conditions after 9 s from the start. Please note that in the Fig. 4, the biomass phase fraction is

shown in logarithmic scale due to the large scale of variation. It can be seen from the figure that gas phase penetrates through the catalyst-biomass bed in form of bubbles, and biomass are evenly dispersed in the fluidized bed.

The velocity fields of different phases in the reactor are shown in Fig. 5, and the amplification of velocity vector of the catalyst phase is shown. It can be seen that the catalyst particles are well fluidized in the reactor with several swirling vortices, which is also applied to spatial distribution of biomass. To better understand the flows of all phases, the vertical directional velocity profiles of gas, catalyst and biomass along the vertical centerline of the reactor are shown in Fig. 6 in which the biomass phase velocity is strongly correlated to the catalyst phase velocity in the bed due to intensive inter-phase momentum exchange. In Fig. 6, the solid velocity fluctuation from -0.25 to +0.25 m/s confirms the fluidization of the particles in the bed. The fluctuated gas velocities through the bed from 0.2 to 0.7 m/s is due to the momentum exchange with the catalyst and biomass, but the gas velocity tends to stabilize above the bed at 0.5 m/s which is slightly higher than the inlet nitrogen velocity due to the contribution of gas product from the pyrolysis process. The abrupt increase in gas velocity at the reactor exit (2.5 m/s) is due to the contraction of cross-section area from exit.

(Insert Fig. 5 here)

(Insert Fig. 6 here)

3.2.2 Temperature distribution within the pyrolysis reactor

Fig. 7 shows the model predicted temperature fields of the gas, catalyst and

biomass phases after 9 s stable operation from the start of biomass feeding. It can be found from the figure that the temperatures of the gas phase and the catalyst phase are uniform at around 773 K, with no observable drop due to the biomass feeding at ambient temperature. This is because the biomass fraction in the bed is very low and its thermal mass is negligible in comparison to gas and catalyst (as shown in Fig. 4). While the temperature of biomass phase is considerably lower than the reactor temperature at the inlet position, it can be heated up quickly by the catalyst and the product gas as it moves within the fluidized bed. The temperature profiles also show that the heat consumption for biomass pyrolysis is low although some reactions are endothermic. This finding has confirmed that some pyrolysis reactions are exothermic as reported in previous studies⁴².

(Insert Fig. 7 here)

3.2.3 Product distribution within the pyrolysis reactor

Fig. 8 shows the mass fraction contour of CFP gaseous products within the reactor in which tar exists in vapor phase however it condenses when being cooled down. It can be observed from the figure that the mass fraction distributions of these components share similar patterns in the bubbling fluidized bed reactor following the gas flow pattern. The mass fractions of the gaseous products are higher near the reactor walls and in the free space above the fluidized bed. This is because the gas vertical velocity along the wall regions is lower than the central zone of the reactor due to the near-wall effect, and thus the gaseous products with longer mean residence time tend to accumulate. In comparison with the non-catalytic pyrolysis simulation

when catalyst loading is zero (results not presented in this paper), the gaseous product distributions are virtually the same although the catalytic cracking reaction of tar is considered. This is because the secondary reaction rate is low and majority components of the product gas are still from primary pyrolysis.

(Insert Fig. 8 here)

3.3 Effects of catalyst structural properties on CFP

The developed model, after validation, has been employed on sensitivity analysis to investigate the effects of the following key catalyst structural properties that are difficult to alter independently in a practical CFP process: (a) The specific surface area of the catalyst particles. (b)The size of the active site. (c)The adsorption constant between tar and catalyst.(d) The tortuosity factor of pores.

The effects of these parameters on biomass CFP performance will be discussed in the following sections. The key criteria of the CFP performance is the catalytic cracking efficiency of tars since it determines the conversion rate of biomass to desired products (organic phase). The mass fractions of products illustrated in following sections are taken as average value over reactor outlet.

3.3.1 Effect of specific surface area of catalyst particle

The specific surface area of the catalyst, the reference value (S_0), was taken as that for the model validation given in Table 2 ($3.0 \times 10^8 \text{ m}^2/\text{m}^3$). The specific surface area is crucial in the biomass CFP as it not only influences the maximum possible

Accepted Article

reaction rate throughout catalytic particle (Equation 22), but also indirectly affects the magnitude of mass diffusion of gases within the catalyst particles (Equations 26-29). Fig. 9 shows the model simulation results for the influences of specific surface area of the catalyst on pyrolysis products distribution and catalytic tar cracking efficiency. In the figure the x-axis is the ratio of catalyst internal surface area (S) to that of the reference value (S_0) in the range from 0.5 to 20. From the figure, it is found that while S/S_0 is changed from 0.5 to 5, the mass fraction of the tar decreases remarkably while the mass fractions of other components of the products (water, char, gas, oil and aqueous) and catalytic cracking efficiency increase. However, when S/S_0 is further increased beyond 5, the mass fractions of products and catalytic tar cracking efficiency change much slowly, approaching constant maximum values at S/S_0 of 10 at which point the corresponding d_{pore} becomes 0.32 nm and the catalytic tar cracking efficiency is 36%. The reason for this is that specific surface area S and pore size d_{pore} of the catalyst are reciprocals (Equation 29), the former determines the theoretical maximum reaction rate, R_{max} , of the catalytic cracking (Equation 22) and the latter influences the internal diffusion of tar vapor through the pores (Equations 26-28). For diffusion of gaseous species in porous media, Knudsen diffusion, which flux is proportional to pore diameter d_p , becomes dominant when pore size is less than 60 nm⁴³. From the model simulation results, it is found that the largest pore size is 6 nm, which is 0.5 time of the reference value of S_0 . Therefore with increase of the S value, the available reaction surface area is increased for catalytic tar cracking, and the internal transportation rate of tar vapor through the pores is decreased with reduction

Accepted Article

in d_{pore} , and vice versa. Therefore, the overall catalytic reaction rate, which is the combination of these two competing effects, can be promoted by increasing S in the situation that Knudsen diffusion is not the rate determining step ($d_{\text{pore}} > 2 \text{ nm}$). In this case, the reaction rate maintains relatively constant when d_{pore} is in the order of magnitude of 0.1 nm (extremely small Knudsen diffusion), and this explains the occurrence of maxima in the catalytic tar cracking efficiency. In reality, the specific surface area of the catalyst may be altered by changing the porosity of catalyst structure to gain optimum performance for catalytic fast pyrolysis.

(Insert Fig. 9 here)

3.3.2 Effect of adsorption constant of tar on catalyst surfaces

Adsorption constant, K_a , of tar vapor on the catalyst surfaces reflects the amount of tar molecules being adsorbed on the catalyst surface, and is thus directly related to the theoretical maximum reaction rate of catalytic tar cracking as shown in Equation (22). K_a is an intrinsic physiochemical property of catalyst and reflects the tar adsorption capability or selectivity of catalyst. This constant is a function of a number of factors including raw materials, recipe of the catalyst or preparation methods of the catalyst. However how the K_a changes with these factors are beyond the scope of this study. Fig.10 shows the model simulation results of tar cracking efficiency and mass yields of biomass pyrolysis products as a function of ratio of the adsorption constant to the reference value $K_a/K_{a,0}$. The reference value of $K_{a,0}$ was taken as $10^{-7} \text{ g}/(\text{g}\cdot\text{Pa})$ which was used in the validation simulation. From Fig. 10, it is found that with

$K_a/K_{a,0}$ increasing from 0.5 to 5, the mass fraction of tar compounds decreases gradually while the fractions of other products increase, and this is particularly remarkable for water and aqueous. In the meantime, the catalytic cracking efficiency of the tar compounds increases linearly from 10 to 30% with $K_a/K_{a,0}$ from 0.5 to 2 which follows the relationship given by Equation (22). With further increase in $K_a/K_{a,0}$ from 2 to 5, the enhancement of catalytic cracking efficiency slows down, increasing from 30% to 45%. This can be explained by the fact that at high intrinsic reaction rate of tar cracking, the mass transfer resistance becomes more influential on R_{\max} . Unlike S, the increase in K_a will not directly affect the internal mass transfer, the catalytic cracking efficiency increases in a square root function pattern with respect to K_a in which no local maxima is expected.

(Insert Fig. 10 here)

3.3.3 Effect of average size of active sites of the catalyst

In the micro-scale structure of the catalyst, the size of active site, D_{AC} , is the mean reactive area required by the specified reaction which reflects the catalytic ability per unit surface area of the catalyst. In general, with larger average size of active site, the number concentration of active sites for a given catalyst volume becomes smaller, hence the catalytic reaction rate will be slower. The number concentration is reciprocal to the square of active site size (Equation 22). However in this work, the active site size was used as the variable parameter as D_{AC} value is comparable with size of gaseous molecules, and it would be explicit to illustrate that the catalyst

Accepted Article

configuration does not fall in the repulsive occupation regime in which occupation will no longer increase with the site concentration. In the base-case simulation, the reference active site size, $D_{AC,0}$, was taken as 3×10^{-10} m (0.3 nm, fringe of gas molecule repulsive interactions become significant) which was used in the model validation simulation. The effect of D_{AC} as the ratio of $D_{AC}/D_{AC,0}$ on the biomass CFP performance is shown in Fig. 11 from the model simulation. From the figure, it is found that the catalytic cracking efficiency of the tar compounds reduces dramatically from 22 to 7% with increasing the size of the active site from 0.3 to 0.6 nm ($D_{AC}/D_{AC,0}$ from 1 to 2). However, with further increase in D_{AC} from 0.6 to 0.9 nm ($D_{AC}/D_{AC,0}$ from 2 to 3), the catalytic cracking efficiency of tar drops to below 4%. This pattern of reduction of tar cracking efficiency with $D_{AC}/D_{AC,0}$ also applies to the mass fractions of biomass CFP final products, as shown in Fig.11. This trend can be explained from Equation (22) which indicates that the theoretical maximum reaction rate of catalytic tar cracking is inversely proportional to the square of D_{AC} . Therefore smaller average active site size is beneficial to catalytic tar cracking efficiency, and increase in number concentration of active site is a possible way to improve the CFP performance. On the opposite trend, the tar mass fraction in the biomass CFP products increases with increasing $D_{AC}/D_{AC,0}$ as less tar compounds are cracked when the size of active site is increased. The value of D_{AC} reflects the number concentration of active sites per catalyst volume, and it may be reduced by increasing the amount of active components (e.g. noble metals) or improve their dispersion in the stage of catalyst preparation.

(Insert Fig. 11 here)

3.3.4 Effect of pore tortuosity factor

The catalytic cracking reaction of tar can take place both on the particle outer surfaces and on the internal pore surfaces of the catalyst^{44,45}. In reality, the non-cylindrical irregularity, curvature channels for instance, in pore geometry creates additional mass transfer resistance within the catalyst particle. To quantify the internal diffusion resistance due to geometrical irregularity of pores of the catalyst, the tortuosity factor of the pores (τ) is introduced which is defined as the ratio of average fluid pathway length through pores to a straight pathway channel over the same distance. Therefore, the tortuosity factor of the perfect cylindrical pores is equal to 1 while the curved pores have the tortuosity factor greater than 1. In this study slightly tortuous pores ($\tau=1.2$) were assumed for start as on average, as slightly tortuous pores could be observed in microscopic characterization of catalyst, and the impact of tortuosity was then investigated using the developed model. In the sensitivity analysis, the ratio (τ/τ_0) of tortuosity factor to the reference value, which was given in Table 2, was investigated for the effects of tortuosity factor on biomass CFP performance, and the results are shown in Fig. 12. It can be seen from the figure that the tar mass fraction increases with τ while yields of other products decrease slightly. This is because the curvatures in the pores reduce the effective diffusion of the tar vapors through the catalyst particle, hence the overall reaction rate of catalytic tar cracking is reduced. However, the effect of tortuosity on catalytic cracking of tar is less significant

compared to other previously mentioned factors. This can be observed from the catalytic cracking efficiency change, which is decreased from 21% to 19% with τ/τ_0 increasing from 1 to 4, and is further decreased to 13% with 10 fold increase in τ .

(Insert Fig. 12 here)

3.4 Effect of external mass transfer on the apparent surface of catalyst

In this study, the effect of external mass transfer from bulk gas phase to the apparent surface of the catalyst in biomass CFP process was investigated by the using the developed model. The results are shown in Fig. 13 in which the product fractions and catalytic tar cracking efficiency are plotted against the ratio of external mass transfer coefficient to the base-case simulation value quantified with k/k_0 varying from 0.1 to 10. From Fig. 13, it can be seen that the impact of varying k is not significant in comparison to other parameters, as mass fraction of tar is decreasing slightly while yield of other products and the catalytic cracking efficiency of tar increases slightly (3%) with increasing k by 100 times (0.1 to 10). In Equation (30), f_{mt} is introduced as the relative effect of external mass transfer resistance on overall volumetric rate of tar cracking. It can be seen from Equation (30) that when k is large enough, value of f_{mt} approaches to 1 and will hardly change with further increasing k . This implies that when the external mass transfer resistance is negligible, the overall catalytic reaction rate will not depend on k . In this study, the base-case simulation average f_{mt} was found to be 0.95 within the fluidized bed, this indicates the external mass transfer k is large enough to overcome the external mass transfer resistance due to small catalyst

diameter. Therefore in the scope of this study, the catalytic tar efficiency increases slightly with k .

(insert Fig. 13 here)

3.5 Comparison of impacts of factors influencing CFP

In the above sections, the impacts of a number of catalyst structural properties on biomass CFP performance have been investigated. In terms of the catalytic tar cracking efficiency, the order of impacts of these properties is found to be: 0.257 for the adsorption constant K_a , 0.226 for the size of active site D_{AC} , 0.124 for the specific surface area S , 0.038 for the tortuosity factor of the pores τ , and 0.011 for the external mass transfer coefficient k . The catalytic tar cracking efficiency is most sensitive to adsorption constant, and biomass CFP performance could be improved tremendously by increasing K_a . In comparison with catalyst structural properties, external mass transfer is a negligible factor to influence the biomass CFP performance.

4. Conclusion

In this study, a CFD model has been developed to simulate the catalytic fast pyrolysis of biomass (CFP) in a laboratory scale bubbling fluidized bed. In the developed model, sophisticated catalyst tar cracking mechanism, which is related to intrinsic chemical reactions, mass transfer and catalyst structural properties, has been proposed and embedded into the reactive multi-phase flow model. The model can be used to better understand the CFP process and to investigate the impacts of catalyst

structural properties as well as mass transfer on the performance of biomass CFP.

The developed model has been experimentally validated by the CFP of pine sawdust. The developed model also has been compared with previously reported model. It is found that the model developed in this study can give more accurate predictions which is attributed to the inclusion of the secondary catalytic cracking of tars, which is related to the microstructural properties of the catalyst.

Parameter study has been carried out to examine impacts of catalyst structural properties on the tar cracking efficiency of the process. The model simulation results show that the CFP performance, in term of tar cracking efficiency, changes monotonically with the investigated properties except for the specific surface area. The optimum specific surface area for this case is about $3.0 \times 10^9 \text{ m}^2/\text{m}^3$, which is 10 times of the reference value used in the base-case simulation, and the corresponding maximum efficiency was found to be 36%.

The order of impacts of the catalysts properties on the overall CFP performance of biomass in bubbling fluidized bed is found to be: adsorption constant > size of the active site > specific surface area > tortuosity > external mass transfer. This implies tar adsorption selectivity of tar vapor should be taken into account as a key parameter in the future design of biomass CFP catalyst. The tortuosity of pores slows down the overall reaction rate by hindering tar vapor diffusion within the catalyst structure. The effect of external mass transfer between the bulk gas phase and the catalyst surface was found to have the least influence on the CFP performance because the mass transfer resistance in this study is found to be insignificant.

References

1. Papadikis K, Gu S, Bridgwater AV. CFD modelling of the fast pyrolysis of biomass in fluidised bed reactors. Part B. *Chemical Engineering Science*. 2009;64(5):1036-1045.
2. Kan T, Strezov V, Evans TJ. Lignocellulosic biomass pyrolysis: A review of product properties and effects of pyrolysis parameters. *Renewable and Sustainable Energy Reviews*. 2016;57:1126-1140.
3. Wright MM, Daugaard DE, Satrio JA, Brown RC. Techno-economic analysis of biomass fast pyrolysis to transportation fuels. *Fuel*. 11/1/ 2010;89, Supplement 1:S2-S10.
4. Ou L, Li B, Dang Q, Jones S, Brown R, Wright MM. Understanding uncertainties in the economic feasibility of transportation fuel production using biomass gasification and mixed alcohol synthesis. *Energy Technol*. 2016;4(3):441–448.
5. Veses A, Aznar M, Martinez I, et al. Catalytic pyrolysis of wood biomass in an auger reactor using calcium-based catalysts. *Bioresource technology*. Jun 2014;162:250-258.
6. Galadima A, Muraza O. In situ fast pyrolysis of biomass with zeolite catalysts for bioaromatics/gasoline production: A review. *Energy Conversion and Management*. 11/15/ 2015;105:338-354.
7. Chen L, Yong SZ, Ghoniem AF. Oxy-fuel combustion of pulverized coal: characterization, fundamentals, stabilization and CFD modeling. *Progress in Energy & Combustion Science*. 2012;38(2):156–214.
8. Menon KG, Patnaikuni VS. CFD simulation of fuel reactor for chemical looping combustion of Indian coal. *Fuel*. 2017;203:90-101.
9. Gerber S, Behrendt F, Oevermann M. An Eulerian modeling approach of wood gasification in a bubbling fluidized bed reactor using char as bed material. *Fuel*. 2010;89(10):2903-2917.
10. Slezak A, Kuhlman JM, Shadle LJ, Spenik J, Shi S. CFD simulation of

entrained-flow coal gasification: Coal particle density/sizefraction effects. *Powder Technology*. 2010;203(1):98-108.

11. Singh RI, Brink A, Hupa M. CFD modeling to study fluidized bed combustion and gasification. *Applied Thermal Engineering*. 2013;52(2):585-614.

12. Xue Q, Heindel TJ, Fox RO. A CFD model for biomass fast pyrolysis in fluidized-bed reactors. *Chemical Engineering Science*. 2011;66(11):2440-2452.

13. Subramanyam MD, Gollakota ARK, Kishore N. CFD simulations of catalytic hydrodeoxygenation of bio-oil using Pt/Al₂O₃ in a fixed bed reactor. *RSC Adv*. 2015;5(110):90354-90366.

14. Gollakota ARK, Subramanyam MD, Kishore N, Gu S. CFD simulations on the effect of catalysts on the hydrodeoxygenation of bio-oil. *RSC Adv*. 2015;5(52):41855-41866.

15. Xiong Q, Zhang J, Xu F, Wiggins G, Stuart Daw C. Coupling DAEM and CFD for simulating biomass fast pyrolysis in fluidized beds. *Journal of Analytical and Applied Pyrolysis*. 1// 2016;117:176-181.

16. Chen S, Fan Y, Yan Z, Wang W, Lu C. CFD simulation of gas–solid two-phase flow and mixing in a FCC riser with feedstock injection. *Powder Technology*. 1// 2016;287:29-42.

17. Mellin P, Kantarelis E, Yang W. Computational fluid dynamics modeling of biomass fast pyrolysis in a fluidized bed reactor, using a comprehensive chemistry scheme. *Fuel*. 2014;117:704-715.

18. Xue Q, Dalluge D, Heindel TJ, Fox RO, Brown RC. Experimental validation and CFD modeling study of biomass fast pyrolysis in fluidized-bed reactors. *Fuel*. 2012;97:757-769.

19. Papadikis K, Gu S, Fivga A, Bridgwater AV. Numerical Comparison of the Drag Models of Granular Flows Applied to the Fast Pyrolysis of Biomass. *Energy & Fuels*. 2010;24(3):2133-2145.

20. Papadikis K, Gu S, Bridgwater AV. Computational modelling of the impact of particle size to the heat transfer coefficient between biomass particles and a fluidised bed. *Fuel Processing Technology*. 2010;91(1):68-79.

21. Papadikis K, Gu S, Bridgwater AV, Gerhauser H. Application of CFD to model fast pyrolysis of biomass. *Fuel Processing Technology*. 2009;90(4):504-512.
22. Papadikis K, Gu S, Bridgwater AV. CFD modelling of the fast pyrolysis of biomass in fluidised bed reactors: Modelling the impact of biomass shrinkage. *Chemical Engineering Journal*. 2009;149(1-3):417-427.
23. Papadikis K, Bridgwater AV, Gu S. CFD modelling of the fast pyrolysis of biomass in fluidised bed reactors, Part A: Eulerian computation of momentum transport in bubbling fluidised beds. *Chemical Engineering Science*. 2008;63(16):4218-4227.
24. Dong N. *CFD Modelling of the Thermal Degradation of Biomass in Fluidized Beds*: School of Engineering Sciences, University of South Hampton; 2014.
25. Sun D, Gu S, Papadikis K. CFD Modeling of the Catalytic Pyrolysis of Biomass With Zeolite in Fluidized Bed. *AIChE Annual Meeting*. San Francisco, CA2013.
26. Geldart D. "Type of Gas Fluidization,". *Powder Technology*. 1973;7(5):285-292.
27. ANSYS Inc. ANSYS FLUENT Theory Guide. *Release 16.0*, 2015.
28. Gidaspow D, Bezburuah R, Ding J. Hydrodynamics of Circulating Fluidized Beds: Kinetic Theory Approach. *Engineering*. 1991.
29. Wen CY, Yu YH. Mechanics of Fluidization. *Chem.engng Prog.symp.ser*. 1966;62:100-111.
30. Syamlal M, Rogers W, O'Brien TJ. Multiphase flow with interphase exchanges (MFIx) documentation theory guide. *Nasa Sti/recon Technical Report N*. 1993;94.
31. Lun CKK, Savage SB, Jeffrey DJ, Chepurini N. Kinetic theories for granular flow: inelastic particles in Couette flow and slightly inelastic particles in a general flow field. *Journal of Fluid Mechanics*. 1984;140(140):223-256.
32. Gunn DJ. Transfer of heat or mass to particles in fixed and fluidised beds. *International Journal of Heat & Mass Transfer*. 1978;21(4):467-476.
33. Ranz WE, Marshall WR. Evaporation from Droplets: part I and II. *Chemical Engineering Progress*. 1952;48:141-173.
34. Chan WCR, Kelbon M, Krieger BB. Modelling and experimental verification of physical and chemical processes during pyrolysis of a large biomass particle ☆. *Fuel*. 1985;64(11):1505-1513.

35. Blasi CD. Heat, momentum and mass transport through a shrinking biomass particle exposed to thermal radiation. *Chemical Engineering Science*. 1996;51(7):1121-1132.
36. Blasi CD, Branca C. Kinetics of Primary Product Formation from Wood Pyrolysis. *Industrial & Engineering Chemistry Research*. 2001;40(23):5547-5556.
37. Perry RH, Green DW, Maloney JO. *Perry's Chemical Engineerings' Handbook*. 7th ed. New York: McGraw-Hill; 1997.
38. Li Y, Zhang C, Liu Y, Hou X, Zhang R, Tang X. Coke Deposition on Ni/HZSM-5 in Bio-oil Hydrodeoxygenation Processing. *Energy & Fuels*. 2015;29(3):1722-1728.
39. Blondeau J, Jeanmart H. Biomass pyrolysis at high temperatures: Prediction of gaseous species yields from an anisotropic particle. *Biomass & Bioenergy*. 2012;41(41):107-121.
40. Zhang C, Zhang R, Li X, et al. Bench-scale fluidized-bed fast pyrolysis of peanut shell for bio-oil production. *Environmental Progress & Sustainable Energy*. 2011;30(1):11-18.
41. Atutxa A, Roberto A, Gayubo A, O.Martin, Javier B. Kinetic Description of the Catalytic Pyrolysis of Biomass in a Conical Spouted Bed Reactor. *Energy & Fuels*. 2005;19:765-774.
42. Blasi CD, Branca C, Galgano A. On the Experimental Evidence of Exothermicity in Wood and Biomass Pyrolysis. *Special Issue: Pyrolysis for Energy Technologies*. 2017;5(1):19-29.
43. He W, Lv W, Dickerson JH. *Gas Diffusion Mechanisms and Models*: Springer International Publishing; 2014.
44. Zhang Y, Chen P, Lou H. In situ catalytic conversion of biomass fast pyrolysis vapors on HZSM-5. *Journal of Energy Chemistry*. 5// 2016;25(3):427-433.
45. Hoff TC, Gardner DW, Thilakaratne R, Proano-Aviles J, Brown RC, Tessonnier J-P. Elucidating the effect of desilication on aluminum-rich ZSM-5 zeolite and its consequences on biomass catalytic fast pyrolysis. *Applied Catalysis A: General*. 1/5/ 2017;529:68-78.

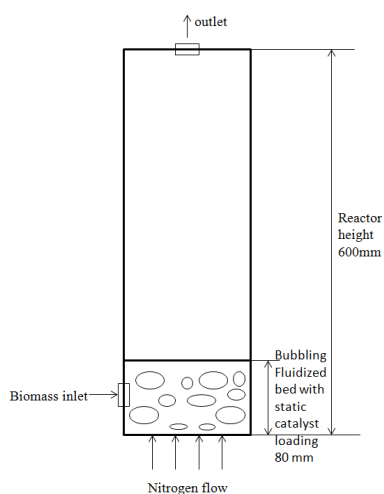


Fig. 1. Schematic diagram of bubbling fluidized bed reactor for the CFD modelling.

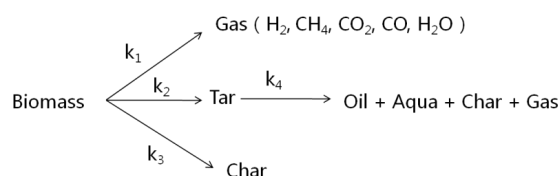


Fig. 2. Reaction pathway scheme and kinetics of biomass catalytic fast pyrolysis

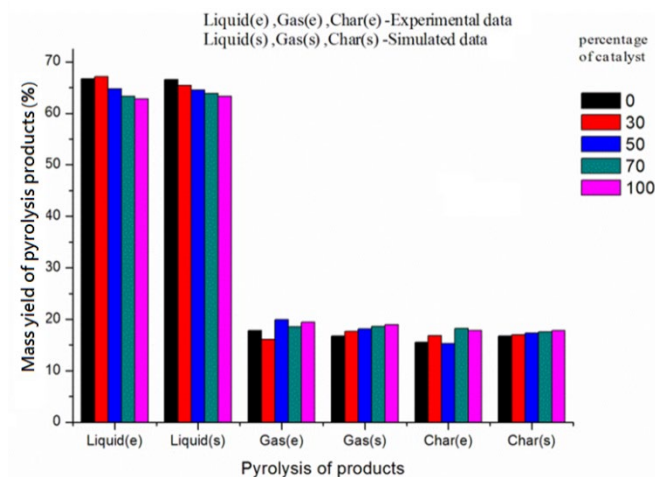


Fig. 3. Comparisons of predicted product yields from the CFP model developed in the present study (with indicator of 's') with the experiment data (with indicator of 'e') at different catalyst blending ratios.

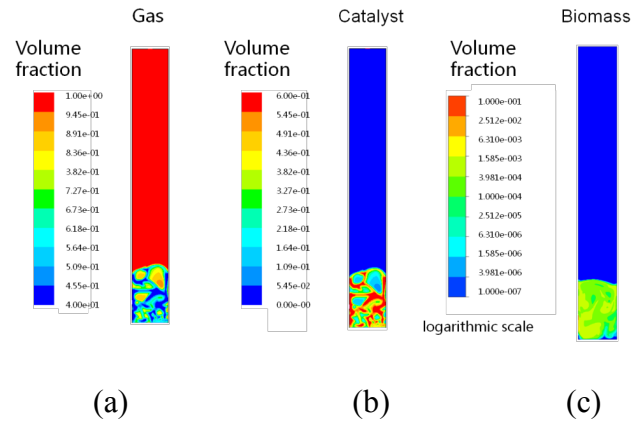


Fig. 4. The model simulated results of volume fraction of (a) gases, (b) catalyst and (c) biomass the different phases for biomass CFP in the bubbling fluidized bed at steady operation conditions after 9 s from the biomass feeding start.

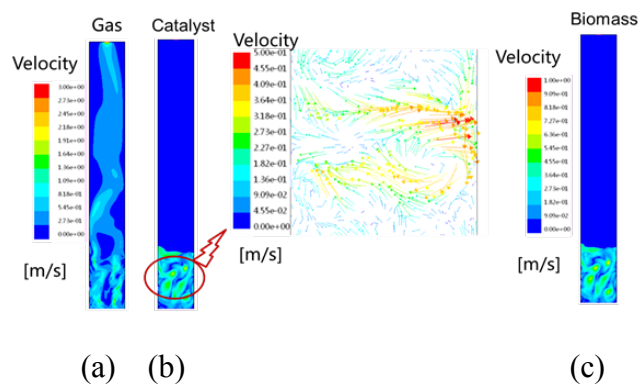


Fig. 5. The model predicted velocity fields of (a) gases, (b) biomass and (c) catalyst for biomass CFP in the bubbling fluidized bed after 9 s from the start.

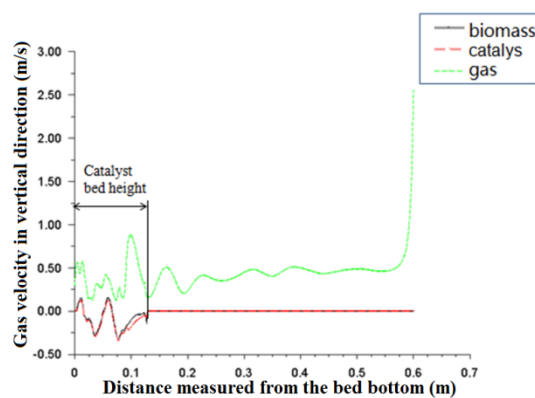


Fig. 6. Model predicted vertical velocity profiles of gas, catalyst and biomass along the vertical centerline for biomass CFP in the bubbling fluidized bed after 9 s from the

start.

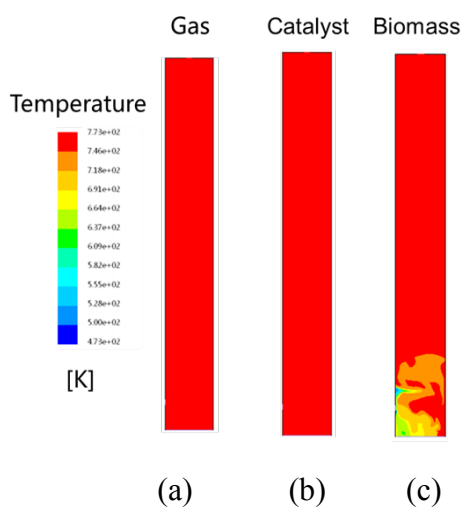


Fig. 7. Model predicted temperature fields of (a) gases, (b) catalyst and (c) biomass in the bubbling fluidized bed reactor at 9 s from the feeding start (temperature of 773 K of phases above the bed is due to initialization of solution).

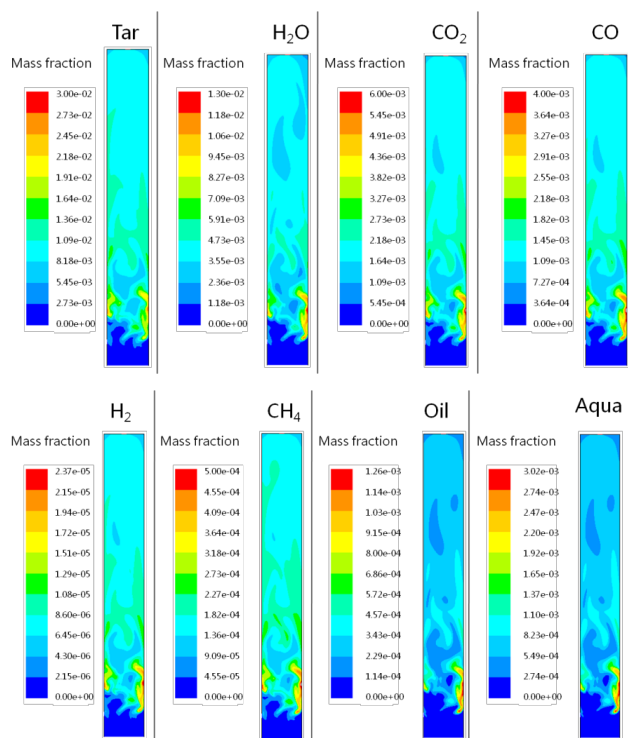


Fig. 8. Model predicted mass fraction contours of gas phase components in the pyrolysis reactor after 9 s from the start.

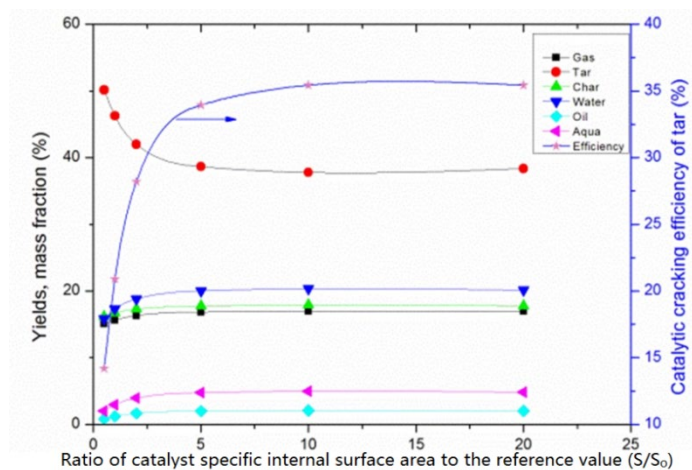


Fig. 9: Model predicted pyrolysis products distributions and catalytic tar cracking efficiency as a function specific internal area of catalyst represented by S/S_0 .

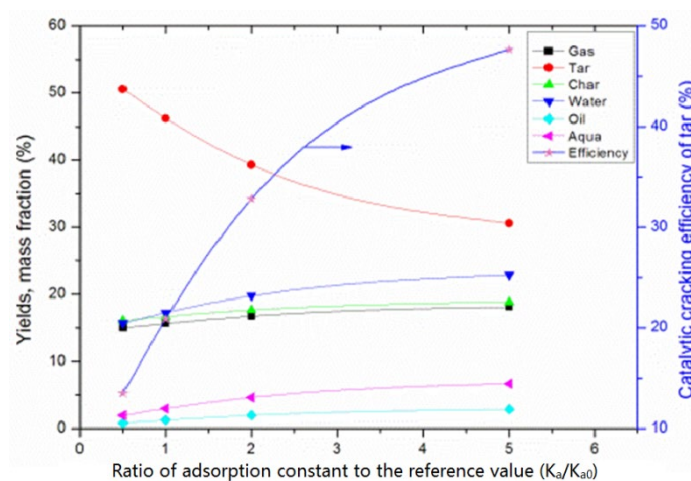


Fig. 10: Model simulated yields of biomass pyrolysis products and catalytic cracking efficiency of tar as a function of adsorption constant of tar on the catalyst surfaces.

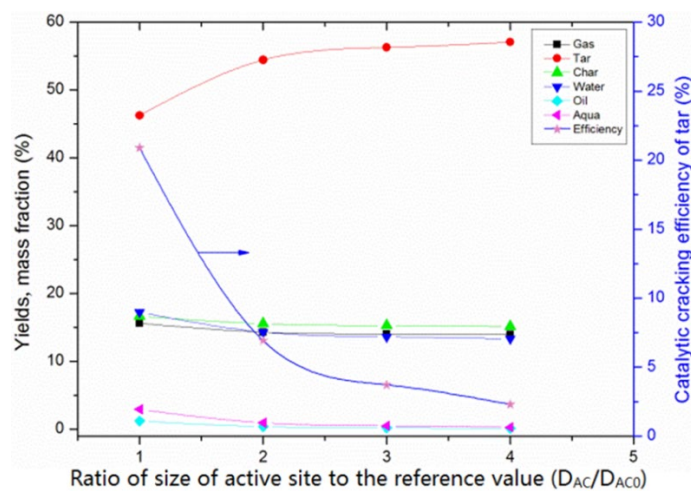


Fig. 11. Model simulated results of products distributions and catalytic cracking efficiency of tar from biomass CFP as function of average size of active sites.

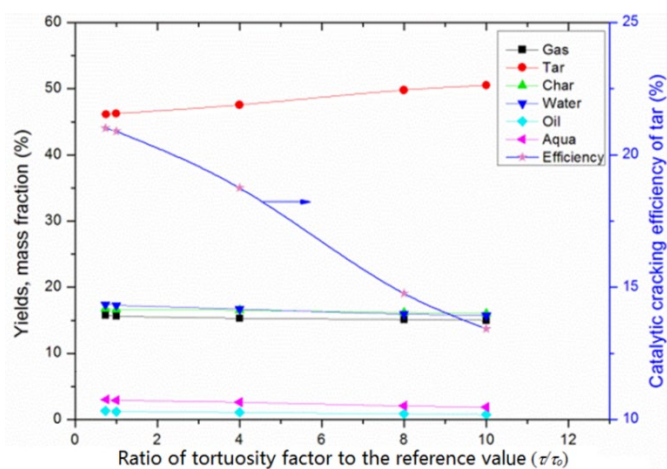


Fig. 12. Model predicted results for the effects of tortuosity factor of catalyst pores on product distributions and catalytic cracking efficiency of tar in biomass catalytic fast pyrolysis.

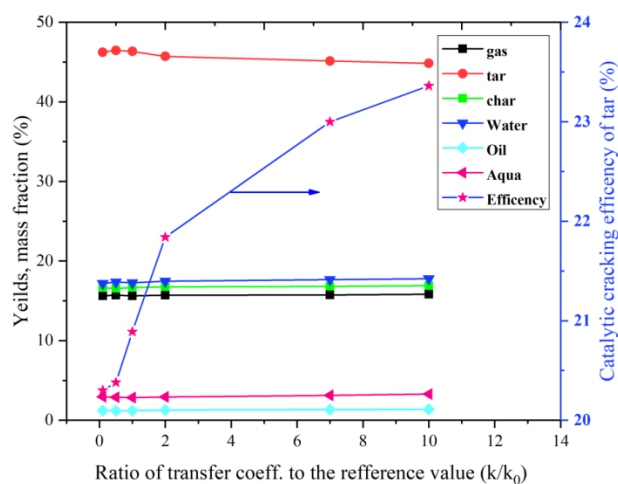


Fig. 13 Pyrolysis products distributions and catalytic cracking efficiency of tar as function of film mass transfer coefficient.

Name	Description	Unit
Greek and Roman symbols		
U_0	reactor superficial velocity	m/s
U_{mf}	minimum fluidizing velocity	m/s
α	volume fraction of phase	(-)
ρ	density	kg/m ³
\dot{m}	interphase mass exchange rate	kg/m ³ /s
S	user-defined mass/energy source	kg/J m ⁻³ s ⁻¹
Y	mass fraction of species	(-)
\vec{v}	velocity vector	m/s
p	pressure	Pa
$\bar{\tau}$	viscous stress tensor	Pa
g	gravitational force	m/s ²
K	interphase momentum exchange coefficient	kg/m ³ /s
v_r	terminal velocity correlation	(-)
d	diameter	m
C_D	drag coefficient	(-)
e	the coefficient of restitution	(-)
C_{fr}	friction coefficient between solid particles	(-)
g_0	solid particle radial distribution coefficient	(-)
h	specific enthalpy	J/kg
h	heat transfer coefficient	W/m ² /K
\vec{q}	heat flux	W/m ²
a	volumetric specific interfacial area	m ² /m ³
λ	thermal conductivity	W/m/K
C_p	heat capacity	J/kg/K
μ	viscosity	Pa·s
k	reaction kinetic constant	s ⁻¹
k	external mass transfer coefficient	m/s
A	pre-exponential factor of reaction	s ⁻¹
E_a	activation energy of reaction	kJ/mol
R	universal gas constant	J/mol/K
T	temperature	K
C_{TS}	specific total concentration of site	mol/m ³
R	volumetric reaction rate	mol/m ³ /s
η	effective factor of volumetric reaction rate	(-)
f_{mt}	mass transfer correction factor	(-)
ε	void fraction	(-)
S	specific surface area	m ² /m ³
D_{AC}	average size of the active site	nm
θ	surface occupation fraction	(-)
K_a	adsorption constant	Pa ⁻¹
V	volume	m ³

C	molar concentration	mol/m ³
ϕ	Thiele modulus	(-)
D	mass diffusivity	m ² /s
τ	pore tortuosity factor	(-)
x	component molar fraction	(-)

Subscripts

i	specie index
g	gas phase
s	bed material phase
w	biomass phase
cata	catalyst
Kn	Knudsen diffusivity
pore	catalyst micro-pore

Dimensionless

Re	Reynolds number
Nu	Nusselt number
Pt	Prandtl Number
Sc	Schmidt Number

Table 1: Reaction kinetics parameters of primary thermal pyrolysis ³⁶.

Reaction	A (1/s)	E _a (kJ/mol)
Biomass → Gas (k ₁)	4.38×10^9	148
Biomass → Tar (k ₂)	1.08×10^{10}	153
Biomass → Char (k ₃)	3.27×10^6	112

Table 2: Catalysts structural properties for HZSM-5 and tar cracking reaction kinetic parameters for base-case model simulation

Structural parameters of the catalysts	Value (unit)
Void fraction of catalyst (ϵ)	0.242(-) ³⁸
Tortuosity factor of pores (τ)	1.2(-)
Specific internal surface area (S)	3.0×10^8 (m ² /m ³) ³⁸
Diameter of pores (d _{pore})	3.2 (nm) ³⁸
Average size of active sites (D _{AC})	3.0×10^{-10} (m) (0.3 nm)
Adsorption constant of tar (K _a)	1.0×10^{-7} (g/(g·Pa))
Pre-exponential factor (A)	2.73×10^7 (1/s)
Activation energy (E _a)	108 (kJ/mol) ³⁹

Table 3: Physical properties, initial and boundary conditions used in the base-case simulation of catalyst fast pyrolysis

Phase	Parameter	Value (unit)	Comment
Biomass (Pine sawdust)	Density (ρ_w)	600 kg/m ³	
	Particle size (d _w)	0.5 mm	Fixed
	Heat capacity (C _{p,w})	1500 J/(kg·K)	value
	Heat conductivity (λ_w)	0.105 W/m/K	
Bed Material Catalyst/Sand (HZSM-5/ Silicon)	Density(ρ_{cata}/ρ_{sand})	1210/2650 kg/m ³	
	Heat capacity (C _{p,cata} /C _{p,sand})	900/1130 J/kg/K	Fixed
	Particle size (d _{cata} /d _{sand})	0.5/0.23 mm	value
Gas (N ₂ and pyro gas mixture)	Heat conductivity ($\lambda_{cata}/\lambda_{sand}$)	0.25/0.75 W/m/K	
	Viscosity (μ_g)	3.44×10^{-5} kg/(m·s)	773K
	Heat capacity (C _{p,g})	mixing-law	
Initial/Boundary Conditions	Heat conductivity (λ_g)	0.0563 W/m/K	773K
	Pressure-outlet (P _{out})	101.3 kPa	Fixed
	Temperature-inlet (T _{in})	773 K	Nitrogen
	Velocity inlet (U ₀)	0.3 m/s	Nitrogen
	Mass flow rate-inlet (M _{w,in})	2 kg/h	Biomass
	Catalyst loading (H _{static})	0.08 m	Fixed
Initial solid packing($\epsilon_{s,0}$)	0.6	Fixed	

Table 4: Comparisons of predicted product yields with the experiment data of 100% catalyst

Parameters	Mass fraction (%)		
	Simulation results		Experimental data ⁽³⁾
Product yields	Microscopic ⁽¹⁾	Macroscopic ⁽²⁾	
Tar+oil+aqueous	44.03	47.35	43.7±3.2
Gas	18.95	16.41	19.4±1.1
Char	17.76	15.36	17.8±0.6
Water	19.26	20.88	19.1±2.4
Tar Cracking	21	22	
Efficiency (%)			

Note: ⁽¹⁾ Simulation results from the microscopic CFP model developed in this study;

⁽²⁾ Simulation results from the macroscopic CFP model proposed by Dong ²⁴.

⁽³⁾ CFP Experiment of pine sawdust at pyrolysis temperature of 500°C, biomass feeding rate of 2 kg/h and nitrogen feeding rate of 2.2 m³/h.